

# Temperature-dependent lattice dynamics and electronic transitions in $0.93\text{Pb}(\text{Zn}_{1/3}\text{Nb}_{2/3})\text{O}_3\text{-}0.07\text{PbTiO}_3$ single crystals: Experiment and theory

Jinzhong Zhang (张金中),<sup>1,2</sup> Wen-Yi Tong (童文旂),<sup>1</sup> Jiajun Zhu (诸佳俊),<sup>1,2</sup> Jiayue Xu (徐家跃),<sup>3</sup> Zhihua Duan (段志华),<sup>1</sup> Liping Xu (徐丽萍),<sup>1</sup> Zhigao Hu (胡志高),<sup>1,\*</sup> Chun-Gang Duan (段纯刚),<sup>1,2</sup> Xiangjian Meng (孟祥建),<sup>2</sup> Ziqiang Zhu (朱自强),<sup>1</sup> and Junhao Chu (褚君浩)<sup>1,2</sup>

<sup>1</sup>Key Laboratory of Polar Materials and Devices, Ministry of Education, Department of Electronic Engineering, East China Normal University, Shanghai 200241, China

<sup>2</sup>National Laboratory for Infrared Physics, Shanghai Institute of Technical Physics, Chinese Academy of Science, Shanghai 200083, China

<sup>3</sup>School of Materials Science and Engineering, Shanghai Institute of Technology, Shanghai 201418, China

(Received 5 September 2014; revised manuscript received 31 December 2014; published 4 February 2015)

The lattice dynamics and electronic transitions of  $0.93\text{Pb}(\text{Zn}_{1/3}\text{Nb}_{2/3})\text{O}_3\text{-}0.07\text{PbTiO}_3$  (PZN-7%PT) single crystal have been investigated by means of temperature dependence polarized Raman scattering and ellipsometric spectra. The rhombohedral-tetragonal and tetragonal-cubic transformations as well as intermediate temperature are extracted based on the locations, intensity, and linewidths of Raman modes in different geometries. Moreover, the redshift behavior of the electronic transition at about 3.7 eV as a function of temperature follows the Bose-Einstein law. Interestingly, the dramatically different optical responses of PZN-7%PT below 3.7 eV during the phase transitions can be observed experimentally and explained by the first-principles calculations, which reveal the potential application of no-contact optical methods in judging the phase transformations and symmetries of ferroelectric crystals.

DOI: [10.1103/PhysRevB.91.085201](https://doi.org/10.1103/PhysRevB.91.085201)

PACS number(s): 77.80.-e, 78.30.Am, 78.20.-e, 31.15.-p

## I. INTRODUCTION

Recently, perovskite-type solid solutions  $(1-x)\text{Pb}(\text{Zn}_{1/3}\text{Nb}_{2/3})\text{O}_3\text{-}x\text{PbTiO}_3$  (PZN- $x$ PT) have been extensively studied because of their excellent piezoelectric coefficient ( $d_{33} \sim 2500$  pC/N), strain levels reaching 1.7% induced by the field applied along [001], and a high electromechanical coupling coefficient ( $k_{33} > 0.9$ ) near morphotropic phase boundary (MPB) region, which are essential for various technological applications such as ultrasonic transducers, solid actuators, and sonar [1–6]. The MPB is a phase boundary that separates the rhombohedral and tetragonal regions in phase diagram. Specifically, it corresponds to  $x \sim 8\%$ – $10\%$  for PZN- $x$ PT [2]. Accurately, the crystal structure of PZN- $x$ PT is polar rhombohedral phase at room temperature for  $x$  below 8% and polar tetragonal symmetry for  $x$  above 10%. Unfortunately, the structure of PZN- $x$ PT near the MPB region is still a matter of controversy. For example, Noheda *et al.* found that there is a monoclinic phase between rhombohedral and tetragonal symmetries, while La-Orauttapong *et al.* discovered an orthorhombic phase in the ferroelectric PZN-9%PT system [7,8]. In addition, PZN- $x$ PT crystals exhibit relatively large electro-optic and photoelastic coefficients ( $\gamma_{33} \sim 450$  pm/V for PZN-8%PT and  $\gamma_{33} \sim 177$  pm/V for PZN-10%PT single crystals poled along [001]), which are expected to be promising materials for a variety of linear and nonlinear optical devices [9,10]. However, the investigations on optical properties of PZN- $x$ PT are not systematic in both experimental and theoretical aspects, which should be further perfected.

Over the past decade, a number of studies have been attempted to investigate relaxor ferroelectric PZN- $x$ PT (phase transformations, ordered nanoregions, polar order, etc.) by

micro-Raman spectroscopy since direct capacitance measurements of the ferroelectric order are often complicated and hindered by parasitic charges forming at interface and electrodes [11–14]. At high temperature, PZN- $x$ PT has an average  $Pm\bar{3}m$  ( $Z_{\text{prim}} = 1$ ) structure, in which 1:1 composition clusters of  $Fm\bar{3}m$  ( $O_h^5$ ,  $Z_{\text{prim}} = 2$ ) symmetry are present [13]. The optical phonon modes in the prototype cubic phase with NaCl-type chemical B-site ( $Fm\bar{3}m$ ) are  $A_{1g}(\text{R}) + E_g(\text{R}) + 2F_{2g}(\text{R}) + 4F_{1u}(\text{IR}) + F_{1g}(\text{S}) + F_{2u}(\text{S})$ , where R, IR, and S stand for Raman-active, infrared-active, and silent modes, respectively. The optical phonon modes in the corresponding B-site chemically ordered tetragonal  $I4mm$  ( $C_{4v}^9$ ,  $Z_{\text{prim}} = 2$ ) and rhombohedral  $R3m$  ( $C_{3v}^5$ ,  $Z_{\text{prim}} = 2$ ) phases are  $6A_1(\text{R, IR}) + 2B_1(\text{R}) + 2B_2(\text{R}) + 8E(\text{R, IR}) + A_2(\text{S})$  and  $7A_1(\text{R, IR}) + 9E(\text{R, IR}) + 2A_2(\text{S})$ , respectively [15]. It was reported that the variations of  $51\text{ cm}^{-1}$  ( $F_{2g}$ ) and  $777\text{ cm}^{-1}$  ( $A_{1g}$ ) modes in the  $z(xx)z$  and  $z(xy)z$  scattering geometries for PZN-8.5%PT crystal exhibit a rhombohedral-tetragonal transformation at about 350 K followed by a tetragonal-cubic one at about 450 K [12]. Moreover, Waesermann *et al.* found that the doublet near  $50\text{ cm}^{-1}$  observed in the high-temperature  $\bar{z}(xy)z$  Raman spectra of PZN- $x$ PT ( $x = 0\text{--}0.1$ ) can be attributed to two distinct cubic states of Pb ions: Pb1 ions surrounded mainly by  $\text{Nb}^{5+}$  and Pb2 ions surrounded by both  $\text{Zn}^{2+}$  and  $\text{Nb}^{5+}$  ones [11]. Recently, PZN- $x$ PT single crystals have been found to exhibit outstanding optical properties [9,10]. The direct ( $E_{gd} = 3.144\text{ eV}$ ) and indirect ( $E_{gid} = 2.915\text{ eV}$ ) energy gap of the PZN-7%PT crystal were determined based on optical transmission spectra [16]. Moreover, the refractive index in the transparent wavelength range for PZN- $x$ PT single crystals with  $x = 5\%$ ,  $8\%$ , and  $10\%$  were obtained by least square fitting using the Cauchy dispersion. However, the electronic band structures and higher electronic transitions of PZN- $x$ PT in a wider photon energy region have not been reported up

\*zghu@ee.ecnu.edu.cn

to now. The mechanisms of electronic transitions in different phases have not been clarified, even though its phase diagram has been sketched.

The objective of this study was to elucidate temperature dependent lattice dynamics, optical constants, and electronic transitions of PZN-7%PT single crystal close to the MPB region based on the combination of micro-Raman spectroscopy, spectroscopic ellipsometry, and first-principles calculations. First, the variation trends of Raman modes and electronic transitions indicate that the rhombohedral-tetragonal and tetragonal-cubic transformations appear at around 360 and 440 K, respectively. Moreover, optical constants and electronic transition energies were obtained based on spectroscopic ellipsometry. Finally, dielectric constants and physical mechanisms of electronic transitions were extracted with the aid of first-principles calculations.

## II. EXPERIMENTAL DETAILS AND APPROACH

### A. Crystal growth

Relaxor ferroelectric PZN-7%PT single crystals have been grown by a modified Bridgman method using 50 mol % PbO as a flux. A certain ratio of PbO, ZnO, Nb<sub>2</sub>O<sub>5</sub>, and TiO<sub>2</sub> with 99.99% purity was used as raw materials. The mixture was sintered at 850 °C for 8 h in a platinum crucible. The furnace temperature was controlled at about 1200 °C using a proportional integral differential controller. The raw materials were soaked in the high temperature zone for 6 h. Then the platinum crucible begins to drop down from high temperature to low temperature by a lowering mechanism. The lowering rate was set to be about 0.5 mm/h. At the same time, a gas cooling system is applied to induce single nucleation. The lowering mechanism can be stopped working when half of the solution was crystallized. Then the furnace was cooled to room temperature at a rate of 80 °C/h. The details about crystal growth of PZN-7%PT can be found elsewhere [17,18]. The as-grown crystal was cut into about 1 mm thickness wafers perpendicular to the [001] direction and the (001) wafers were polished on both sides to a dimension of 10 × 10 × 1 mm<sup>3</sup>. The chemical composition of the grown crystal is 1:0.30:0.62:0.073:2.99 for Pb:Zn:Nb:Ti:O identified by the energy dispersive x-ray spectroscopy (EDS, using an EDS spectrometer attached to a field emission scanning electron microscopy: FESEM, Philips XL30FEG). It is approximate to the nominal stoichiometric value (1:0.31:0.62:0.07:3).

### B. Structural and optical characterizations

The crystalline structure of PZN-7%PT single crystal was investigated by high resolution x-ray diffraction (HR-XRD) using a Ge(220) filtered Cu *K*α radiation source (D8 DISCOVER, Bruker). In the HR-XRD measurement, a scanning mode ( $\theta$ - $2\theta$ ) was selected with a scanning speed of 0.1 second/step and increment of 0.005°. Temperature-dependent VV (polarizer and analyzer in vertical position) and VH (polarizer in vertical position and analyzer in horizontal position) Raman spectra have been collected on heating by using a micro-Raman spectrometer with a spectral resolution of 1 cm<sup>-1</sup> (Jobin-Yvon LabRAM HR 800 UV) in the temperature range of 80-800 K

with a precision of about 0.5 K. The He-Ne laser with the wavelength of 632.8 nm was taken as the exciting source. The laser beam was focused through a 50× microscope with a working distance of 18 mm. An air cooled charge coupled device (CCD) (-70 °C) with a 1024 × 256 pixels front illuminated chip used to collect the scattered signal dispersed on 1800 grooves/mm grating. All Raman spectra have been dealt with the Bose-Einstein occupation factor [19]. The temperature-dependent ellipsometric spectra were recorded on heating by near infrared-ultraviolet spectroscopic ellipsometry in the photon energy range of 1.5–6.0 eV (V-VASE by J. A. Woollam Co., Inc.). The temperature can be varied from 4 to 500 K using an Instec cell with liquid nitrogen cooling accessory and frame water pump cooling (Janis ST-400). The ellipsometric data were fitted by the software package WVASE32, which allows window corrections to be included as a part of the model during the analysis process.

### C. Theoretical approach

*Ab initio* density functional theory calculations based on the projector augmented wave method are conducted by the Vienna *ab initio* Simulation Package (VASP) [20,21]. Perdew-Burke-Ernzerhof (PBE) form of the generalized gradient approximation (GGA) for exchange and correlation is employed along with a standard plane-wave basis set with a kinetic-energy cutoff of 650 eV. These calculations were performed by using the 11 × 11 × 11 Monkhorst-Pack *k*-point mesh [22], and the convergence criterion for the electronic energy is 10<sup>-6</sup> eV. Considering the quite small density of Ti atoms in PZN-7%PT, we carry out the first-principles density functional optical studies for PZN in order to simplify the calculations. By referring to the theoretical work in similar systems (PbMg<sub>1/3</sub>Nb<sub>2/3</sub>O<sub>3</sub>) [23], the minimal 15 atom hexagonal cells are set to describe the cubic phase as well as the rhombohedral phase with the polar axis along the threefold [001]<sub>h</sub> direction (or equivalently pseudocubic [111]<sub>c</sub> direction). The tetragonal phase, as shown in Fig. 1(c), is established by replicating a perovskite structure three times along its polar axis, i.e., the [001]<sub>c</sub> direction. Proper simulations of plausible local arrangements of B-site Zn and Nb atoms mimicking the experimentally observed chemical order of type Pb(B'<sub>2/3</sub>B''<sub>1/3</sub>)<sub>1/2</sub>B''<sub>1/2</sub>O<sub>3</sub> were not possible due to computational limitations [24]. Hence we used different B-site cation arrangements for different phases in order to construct a cluster containing Zn and Nb atoms in the same ratio 1:2 for all the three phases: 1:2 ordering along the [111]<sub>c</sub> direction for the cubic and rhombohedral phases and 1:2 ordering along the [001]<sub>c</sub> direction for the tetragonal phase. The results of optical calculations are based on the independent-particle approximation using our own code OPTICPACK [25]. The interband optical conductivity tensor can be written as  $\sigma(\omega) = 2\pi/\omega\Omega \sum_{\mathbf{k}} W_{\mathbf{k}} \sum_{c,v} |\langle c | \mathbf{e} \cdot \mathbf{p} | v \rangle|^2 \delta(E_c - E_v - \omega)$ , where  $\omega$  is photon energy,  $\Omega$  is the cell volume,  $\mathbf{e}$  is the polarization direction of photons, and  $\mathbf{p}$  is the electron momentum operator. The imaginary part of complex dielectric functions  $\varepsilon_i(h\nu)$  is evaluated from optical conductivity and the real part  $\varepsilon_r(h\nu)$  can be obtained by the Kramers-Krönig relation.

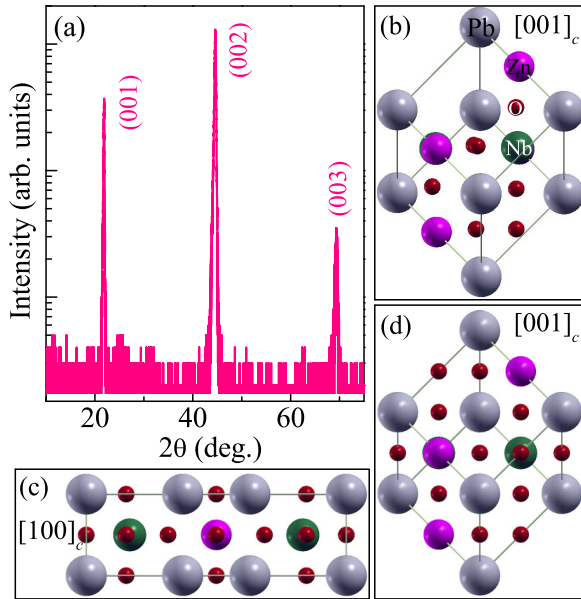


FIG. 1. (Color online) (a) HR-XRD pattern of PZN-7%PT single crystal measured at room temperature and it was plotted as the log scale in intensity. (b) Rhombohedral, (c) tetragonal, and (d) cubic structure for PZN material projected perpendicular to the different directions.

### III. RESULTS AND DISCUSSION

#### A. Crystal structure

Figure 1(a) illustrates the XRD pattern of PZN-7%PT single crystal recorded at room temperature. It suggests that three diffraction peaks (001), (002), and (003) are single without splitting, which indicates that its structure belongs to rhombohedral (so-called pseudocubic) phase with a lattice constant of about  $3.964 \pm 0.040$  Å. According to the phase diagram of PZN-*x*PT, PZN-7%PT undergoes rhombohedral-tetragonal-cubic phase transformations with increasing temperature [8]. Figures 1(b) and 1(d) show rhombohedral and cubic structures of PZN material projected perpendicular to the  $[001]_c$  direction, respectively. On the other hand, the distorted tetragonal structure projected perpendicular to the  $[100]_c$  direction is shown in Fig. 1(c). In contrast with  $\text{PbTiO}_3$ , PZN has an extremely small distortion from cubic and yet has a large polarization [26].

#### B. Polarized Raman scattering

Polarized Raman spectra of (001)-oriented PZN-7%PT single crystal collected at different temperatures in the VV and VH scattering geometries are shown in Figs. 2(a) and 2(b), respectively. Note that all measured Raman spectra have been divided by the Bose-Einstein occupation number  $n(\omega) + 1 = 1/[1 - \exp(-\hbar\omega/k_B T)]$  ( $\hbar$  and  $k_B$  are Planck constant and Boltzmann constant, respectively) to get rid of the trivial temperature dependence [19,27,28]. These spectra in the VV and VH geometries display similar line shapes and do not differ qualitatively except for intensity variations below 400 K. At high temperature above 500 K, there are four main Raman bands located at about 50, 270, 400–600, and 780  $\text{cm}^{-1}$ ,

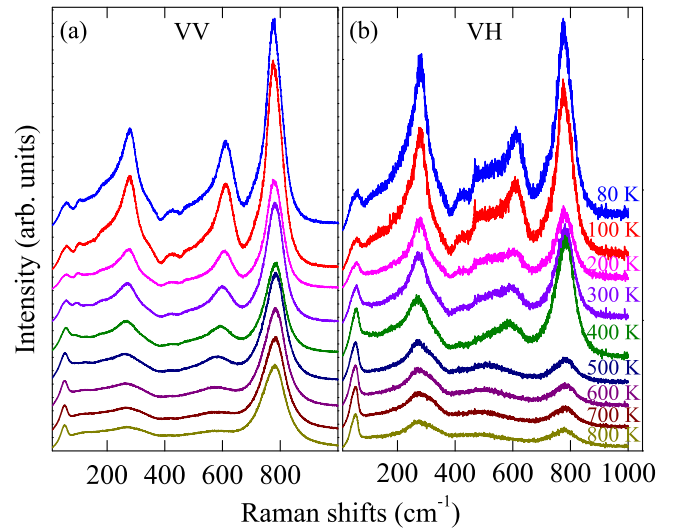


FIG. 2. (Color online) (a) VV and (b) VH Raman scattering of the PZN-7%PT single crystal at different temperatures after correcting for thermal population factor. Note that each spectrum is shifted in intensity for clarity.

respectively. The dominant feature is that the intensity of the band at about 780  $\text{cm}^{-1}$  has a marked decrease in the VH scattering geometry, as compared to that in the VV geometry. Moreover, the band around 600  $\text{cm}^{-1}$  in the VH scattering geometry vanishes at high temperature. These phenomena indicate that the crystal structure changes and there are phase transitions between 400 and 500 K. In addition, all the intensity of Raman scattering decreases on heating.

In order to ascertain the peak positions, intensity, and linewidths [full width at half maxima (FWHM)] of phonon modes, the Raman spectra with different temperatures were decomposed into a series of bands with the assumption of a Lorentzian line shape approximation. For example, the decomposed Raman spectra in the VV and VH configurations at 80, 400, and 800 K are shown in Fig. 3. The fitting spectra are in good agreement with the experimental ones. On the length scale of sensitivity from Raman scattering, the existence of modes at about 50 and 780  $\text{cm}^{-1}$  reveals that the Pb-based relaxor exhibits a double-perovskite structure because they are symmetrically allowed only in a double-perovskite structure. These modes located around 780 and 50  $\text{cm}^{-1}$  originate from the first-order Raman scattering related to cubic Raman-active nondegenerate and triply degenerate modes of the prototype structure, respectively [11]. It suggests that a moderation addition (7%) of PT to PZN does not disturb the double-perovskite structure. Note that more peaks than symmetry-allowed ones are observed above 500 K due to the presence of ferroic atomic arrangements with a lifetime longer than the time-scale sensitivity from Raman spectroscopy.

The band near 50  $\text{cm}^{-1}$  originates from the Pb localized mode, which is a doublet even at high temperature due to the existence of two cubic local states from the Pb ions. The lower wave number component ( $\sim 40$   $\text{cm}^{-1}$ ) arises from the Pb1 ions surrounded by  $\text{Nb}^{5+}$ , which reflects the presence of ferroelectric long-range order. The higher one ( $\sim 60$   $\text{cm}^{-1}$ ) originates from the Pb2 ions surrounded by both  $\text{Zn}^{2+}$  and

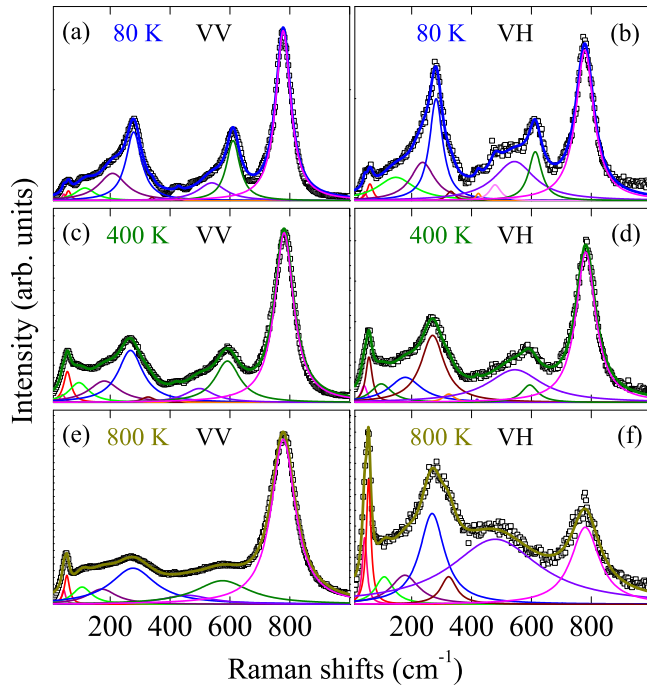


FIG. 3. (Color online) Decomposed Raman spectra for PZN-7%PT crystal at (a),(b) 80 K, (c),(d) 400 K, and (e),(f) 800 K in the VV and VH geometries. The solid lines represent the Lorentzian fitting model.

$\text{Nb}^{5+}$ . Their integrated intensity ratio in the VV geometry as a function of temperature is shown in Fig. 4(a). The rhombohedral (R) to tetragonal (T) phase transition temperature  $T_{\text{RT}} = 360$  K and the intermediate temperature  $T^* = 510$  K are revealed by different variation trends of intensity ratio. The local maxima in the FWHM of the peak near  $60 \text{ cm}^{-1}$  as a function of temperature suggests happening of the ferroelectric tetragonal to paraelectric cubic phase transition  $T_{\text{C}} = 440$  K [Fig. 4(b)]. The temperature-dependent various trends of the intensity ratio and FWHM from the Raman signals near  $50 \text{ cm}^{-1}$  can well suggest the phase transition temperatures ( $T_{\text{RT}}$  and  $T_{\text{C}}$ ) and intermediate temperature ( $T^*$ ). In addition, three temperature points have also been confirmed by the corresponding positions, intensity, and FWHM as a function of temperature from other phonon modes. Accurately, the Raman-active mode near  $270 \text{ cm}^{-1}$  arises from vibrations of off-centered B-site cations. It is sensitive to the development of polar order, which is related to the coupling processes at the intermediate temperature [2]. Figures 4(c) and 4(d) suggest that the phonon mode around  $270 \text{ cm}^{-1}$  in the VH geometry has a shift towards lower wave numbers on heating due to the unit-cell expansion in a single structure and its integrated intensity decreases with some abnormal points. Between different phases, the deduction of intensity on heating may be due to the reduction of polar shifts about B-site cations to a certain extent as well as the unit-cell expansion [2]. Therefore, its intensity value and corresponding slope are the smallest at the temperature region above  $T^*$ . The mode near  $600 \text{ cm}^{-1}$  corresponds mainly to oxygen bending vibrations [13]. Figure 4(e) illustrates that it has a shift towards lower wave numbers in both VV and VH spectra

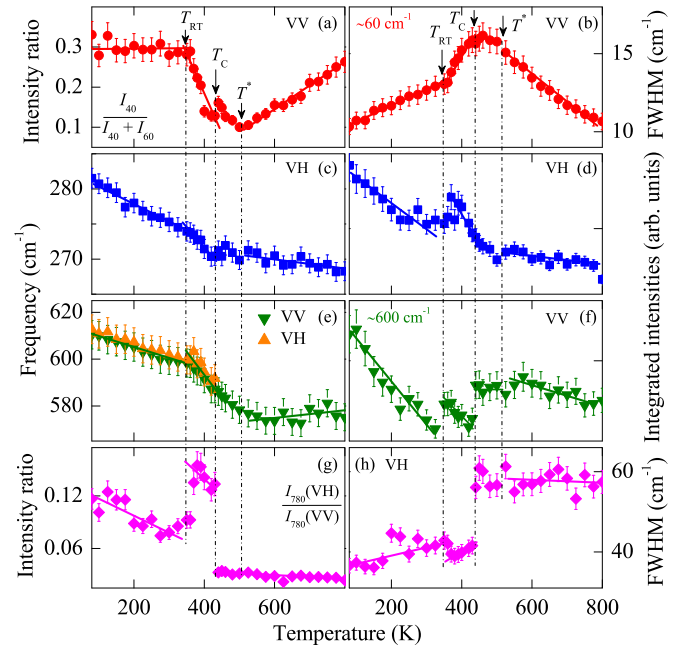


FIG. 4. (Color online) Temperature dependence of (a) integrated intensity ratio  $I_{40}/(I_{40} + I_{60})$  and (b) FWHM of  $\sim 60 \text{ cm}^{-1}$  in the VV geometry. (c) Peak positions and (d) FWHM of  $\sim 270 \text{ cm}^{-1}$  in the VH geometry as a function of temperature. (e) Peak positions in the VV ( $\blacktriangledown$ ) and VH ( $\blacktriangle$ ) geometries, and (f) FWHM in the VV geometry of the mode near  $600 \text{ cm}^{-1}$ . (g) Integrated intensity ratio  $I_{780}(\text{VH})/I_{780}(\text{VV})$  between VH and VV geometries and (h) FWHM in the VH geometry of the mode near  $780 \text{ cm}^{-1}$ . The solid lines are a guide for the eyes to emphasize the various trends and the vertical dash lines are applied to divide the temperature region into various crystal structures.

at low temperature. It vanishes in the VH geometry above  $440 \text{ K}$  ( $T_{\text{C}}$ ), while it has a slight shift towards higher wave numbers above  $510 \text{ K}$  ( $T^*$ ). For the integrated intensity of the Raman mode in the VV geometry, as shown in Fig. 4(f), four temperature regions can be divided by three anomalies at  $360$ ,  $440$ , and  $510 \text{ K}$ , which is corresponding to the  $T_{\text{RT}}$ ,  $T_{\text{C}}$ , and  $T^*$ , respectively.

The Raman mode located at about  $780 \text{ cm}^{-1}$  is strong and its parameters can be extracted well for separation from other modes. It should be further investigated because it reflects the subtle changes in the lattice structure [12,13]. The integrated intensity ratio  $I_{780}(\text{VH})/I_{780}(\text{VV})$  between the VH and VV geometries shows a marked change near  $360$  and  $440 \text{ K}$ , which are corresponding to the R to T and T to C transition temperatures, respectively [Fig. 4(g)]. It is obvious that its integrated intensity in the VH spectra has a sharp decrease above  $T_{\text{C}}$ , as compared to that in the VV spectra. This phenomenon is similar to that of the mode near  $600 \text{ cm}^{-1}$ , which vanishes above  $T_{\text{C}}$  in the VH geometry. The broadening of the mode near  $780 \text{ cm}^{-1}$  in the VH geometry indicates that the volume ratio of ordered and disordered regions decreases on heating. Nevertheless, there is not enough evidence to determine another important temperature point (Burns temperature  $T_{\text{d}}$ ).

### C. Interband electronic transitions

The optical behaviors of the PZN-7%PT single crystal with different phases were investigated by spectroscopic ellipsometry based on the reflectance configuration. It is a sensitive and nondestructive optical technique, which measures the relative changes in the amplitude and phase of particular directions' polarized lights upon oblique reflection from the sample surface. The experimental parameters measured by ellipsometry are the complex ratio  $\tilde{\rho}(h\nu)$  in terms of  $\Psi(h\nu)$  and  $\Delta(h\nu)$ , which are defined as  $\tilde{\rho}(h\nu) \equiv \tilde{r}_p(h\nu)/\tilde{r}_s(h\nu) = \tan \Psi(h\nu)e^{i\Delta(h\nu)}$ ; here,  $\tilde{r}_p(h\nu)$  and  $\tilde{r}_s(h\nu)$  are the complex reflection coefficient of the light polarized parallel and perpendicular to the incidence plane, respectively [29]. Note that  $\tilde{\rho}(h\nu)$  is a function of the incident angle, photon energy  $h\nu$ , and optical functions  $\tilde{\epsilon}(h\nu)$  of measured materials. For a bulk material with idealized surface, its optical functions can be calculated directly:  $\langle \tilde{\epsilon} \rangle = \langle \epsilon_r \rangle + i \langle \epsilon_i \rangle = \sin^2\theta [1 + \tan^2\theta (1 - \tilde{\rho})^2 / (1 + \tilde{\rho})^2]$ ; here  $\theta$  is the incident angle [30]. Actually, an appropriate model has to be assumed for bulk materials with a surface roughness layer and multilayer structures. In order to extract the optical band gap, dielectric functions, and thickness of surface roughness of the PZN-7%PT bulk material, the ellipsometric spectra were fitted by a three-layer structure (air/surface rough layer/PZN-7%PT) based on the Snell's law, Fresnel equation, and the light absorption in the surface rough layer. Specifically, the dielectric constants of the surface roughness are taken into account by the Bruggeman effective medium approximation  $\tilde{\epsilon}_{eff}(h\nu)$ , which is described by the assumption 50% void component  $\tilde{\epsilon}_v(h\nu)$  and 50% PZN-7%PT bulk material  $\tilde{\epsilon}_B(h\nu)$  [i.e.,  $0 = 50\% \frac{\tilde{\epsilon}_v(h\nu) - \tilde{\epsilon}_{eff}(h\nu)}{\tilde{\epsilon}_v(h\nu) + 2\tilde{\epsilon}_{eff}(h\nu)} + 50\% \frac{\tilde{\epsilon}_B(h\nu) - \tilde{\epsilon}_{eff}(h\nu)}{\tilde{\epsilon}_B(h\nu) + 2\tilde{\epsilon}_{eff}(h\nu)}$ ] [31]. Correspondingly, the band structure observed in the dielectric spectra of PZN-7%PT material is attributed to interband transitions, which can be evaluated in terms of standard analytic line shapes (the standard critical point model) defined as [32]:  $\tilde{\epsilon}(h\nu) = C - A e^{i\varphi} (h\nu - h\nu_k + i\Gamma)^n$ . Here, a critical point is described by the amplitude  $A$ , excitonic phase angle  $\varphi$ , electronic transition  $h\nu_k$ , and broadening  $\Gamma$ . Note that the exponent  $n$  has the values of  $-0.5$ ,  $0$  [ $\ln(h\nu - h\nu_k + i\Gamma)$ ], and  $0.5$  for the one-, two-, and three-dimensional critical point. Correspondingly, we calculated numerically the second partial derivative of the dielectric function  $\partial^2 \tilde{\epsilon} / \partial (h\nu)^2$  for showing the electronic transitions in dielectric spectra and performing a line-shape analysis of the critical point as follows:

$$\frac{\partial^2 \tilde{\epsilon}}{\partial (h\nu)^2} = B e^{i\varphi} (h\nu - h\nu_k + i\Gamma)^{n-2}. \quad (1)$$

It should be emphasized that electronic transitions derived from the second partial derivative of dielectric functions are independent of the surface roughness layer, which can affect dielectric function values.

Figure 5(a) shows the experimental ellipsometric spectra  $\Psi(h\nu)$  and  $\Delta(h\nu)$  measured at different temperatures. In the temperature region below 300 K, the  $\Psi(h\nu)$  and  $\Delta(h\nu)$  have similar shapes. As the temperature increases, the variation trends become obvious. For example, the experimental and fitted ellipsometric spectra at 4 and 450 K are plotted in Fig. 5(b). Correspondingly, the thickness of roughness layer was obtained ( $9 \pm 1$  nm) and the derived complex dielectric constants (4 and 450 K) are shown in Fig. 5(c). It suggests

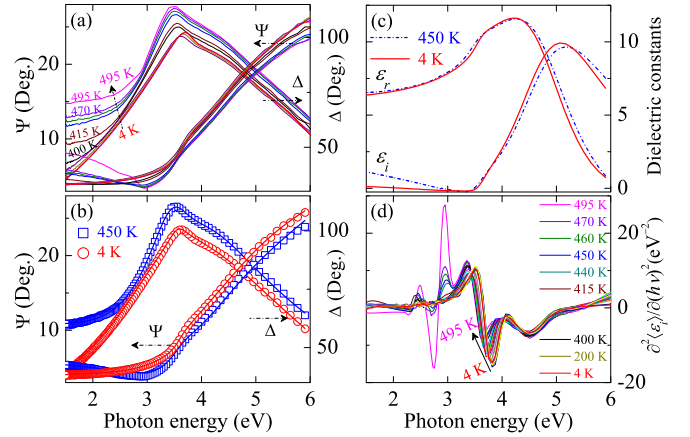


FIG. 5. (Color online) (a) Visible-ultraviolet experimental ellipsometric spectra  $\Psi(h\nu)$  and  $\Delta(h\nu)$  at different temperatures. (b) Experimental (solid lines) and fitted (dotted lines) ellipsometric spectra and (c) evaluated dielectric constants ( $\tilde{\epsilon} = \epsilon_r + i\epsilon_i$ ) at 450 and 4 K. (d) The second partial derivative spectra for the imaginary part of pseudodielectric function from PZN-7%PT single crystal at different temperatures.

that there are some additional electronic transitions in the low energy region since  $\epsilon_i$  is not close to zero at higher temperature. In order to accurately evaluate the electronic transitions of the PZN-7%PT in the photon energy range of 1.5–6.0 eV, the second partial derivative spectra for the imaginary part of pseudodielectric function  $\langle \epsilon_i \rangle$  at different temperatures are calculated, as illustrated in Fig. 5(d). It suggests that there are three transitions at low temperature, while another two transitions in the lower energy region emerge at higher temperature. Moreover, the obvious transition located at about 3.7 eV has a redshift trend with increasing temperature.

To investigate the behavior of electronic transition in PZN-7%PT with different phase transformations, the second partial derivative spectra of the pseudodielectric functions with a series of temperature have been fitted by the standard critical point (SCP) model and the transition energies and corresponding broadenings at different temperatures were listed in Table I. For example, the fitting quality for experimental (dotted lines) and simulative (solid lines)  $\partial^2 \langle \epsilon_i \rangle / \partial (h\nu)^2$  and  $\partial^2 \langle \epsilon_r \rangle / \partial (h\nu)^2$  at the temperatures of 4 and 450 K can be evaluated in

TABLE I. Electronic transitions and broadenings of the PZN-7%PT single crystal at different temperatures.

$T$ (K)	$h\nu_1$ (eV)	$\Gamma_1$ (eV)	$h\nu_2$ (eV)	$\Gamma_2$ (eV)	$h\nu_3$ (eV)	$\Gamma_3$ (eV)	$h\nu_4$ (eV)	$\Gamma_4$ (eV)
4					3.72	0.285	4.46	0.739
100					3.73	0.293	4.54	0.719
200					3.66	0.296	4.59	0.877
250	2.26	0.324			3.64	0.303	4.60	1.004
300	2.30	0.155			3.63	0.308	4.60	1.019
350	2.34	0.242			3.61	0.307	4.56	1.003
400	2.36	0.131			3.55	0.301	4.46	0.977
450	2.39	0.185	2.92	0.196	3.52	0.317	4.33	0.944
500	2.57	0.268	2.89	0.189	3.45	0.327	4.23	0.845

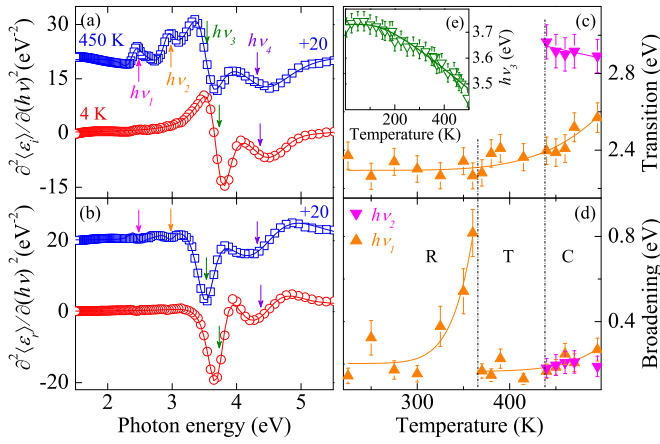


FIG. 6. (Color online) Experimental (dotted lines) and best-fitted (solid lines) second partial derivatives of the (a) imaginary  $\langle \epsilon_i \rangle$  and (b) real  $\langle \epsilon_r \rangle$  parts of pseudodielectric function for PZN-7%PT single crystal at 4 and 450 K, respectively. For clarity, the spectrum with the temperature of 450 K was shifted and the transition energies were marked by arrows. (c) Transition energies and (d) broadenings of  $h\nu_1$  and  $h\nu_2$  as a function of temperature. (e) The transition energy (dotted lines) of  $h\nu_3$  as a function of temperature. The solid lines in (d) and (e) are the fitting results by the Bose-Einstein model.

Figs. 6(a) and 6(b), respectively. At high temperature, two additional peaks ( $h\nu_1$  and  $h\nu_2$ ) in the lower energy region can be simulated well. Based on the analysis of temperature-dependent polarized Raman scattering, the appearance of  $h\nu_2$  at about 440 K indicates a transformation from tetragonal phase to cubic phase, as shown in Fig. 6(c). The  $h\nu_1$  appears at about 250 K since there may be a mixture of rhombohedral and tetragonal phases. Figure 6(d) shows that the broadening response of the  $h\nu_1$  suggests a phase transformation from rhombohedral phase to tetragonal structure at about 360 K, which is consistent with the results of Raman analysis. For the low temperature range, the first electronic transition energy is located at about 3.7 eV and its energy position as a function of temperature was plotted in Fig. 6(e). The temperature dependence for  $h\nu_3$  is not sensitive to phase transformations. It can be well explained by the Bose-Einstein model, which takes into account the electron-phonon interaction and is written as [32–36]  $h\nu_k(T) = h\nu_k(0) - 2a_v/(e^{\Theta_v/T} - 1)$ . For PZN-7%PT single crystal, the transition energy at absolute zero  $h\nu_k(0)$  is about 3.73 eV, the strength of the electron-phonon interaction  $a_v$  is 0.22 eV, and Einstein temperature  $\Theta_v$  is 504 K, respectively.

#### D. Physical mechanism

In order to clarify the causes of the extremely different optical responses below 3.7 eV during the rhombohedral-tetragonal and the tetragonal-cubic phase transitions, theoretical calculations were performed. Figure 7 shows the calculated band structure, partial, and total density of states for  $\text{Pb}(\text{Zn}_{1/3}\text{Nb}_{2/3})\text{O}_3$  with different phases. As a matter of fact, the top of valence bands and bottom of conduction ones consist of mainly O-2p and Nb-4d states, respectively. The higher conduction bands in the range of 3–4 eV originate from mainly Pb-6p and Nb-4d states. Note that there are no

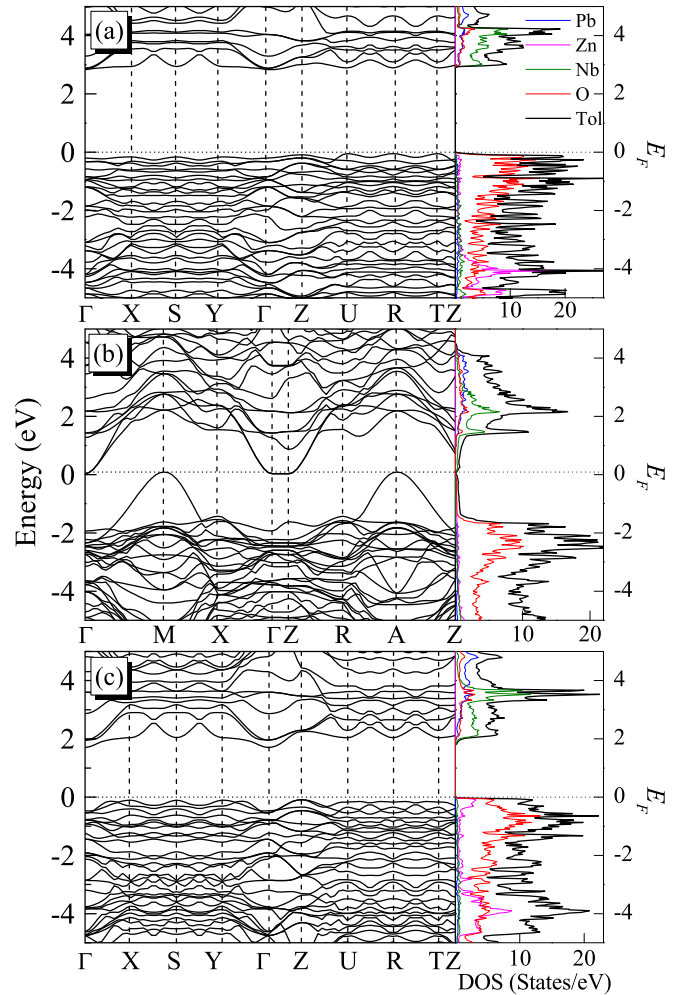


FIG. 7. (Color online) Calculated band structure and corresponding density of states for (a) rhombohedral, (b) tetragonal, and (c) cubic  $\text{Pb}(\text{Zn}_{1/3}\text{Nb}_{2/3})\text{O}_3$ .

states above Fermi energy for Zn-3d, which is similar to the case of Mg-d states in  $\text{Pb}(\text{Mg}_{1/3}\text{Nb}_{2/3})\text{O}_3$  [37]. As shown in Fig. 7(b), the extremely small band gap for tetragonal phase seems to violate the experimental results. Its direct band gap located at the point of symmetry Z (0, 0, 0.5) is approximately 2 eV, which is consistent with optical band gap. However, the band gap is indirect according to its corresponding band structure. As a well-known problem of calculations based on density-functional theory (DFT), the calculated optical band gaps are underestimated by about 20%–30%, as compared to the experimental values. Nevertheless, the relative energy of peaks is in good agreement with the experimental results from the right panels of Fig. 8. Therefore, the present first-principles calculations are reliable and can be used to make qualitative analysis.

In the process of the transformation from rhombohedral phase to tetragonal phase, the corresponding energy of absorption edges changes from 2.63 eV [the cause of  $h\nu_3$  in Fig. 8(b)] to 1.69 eV [the cause of  $h\nu_1$  in Fig. 8(d)]. Detailed analysis shows that the leading interband transitions of the absorption edges derive from O-2p<sub>z</sub> → Nb-4d<sub>xy</sub> for the rhombohedral case and the hybridization O-2p<sub>z</sub> and Pb-6s → Nb-4d<sub>xy</sub> for

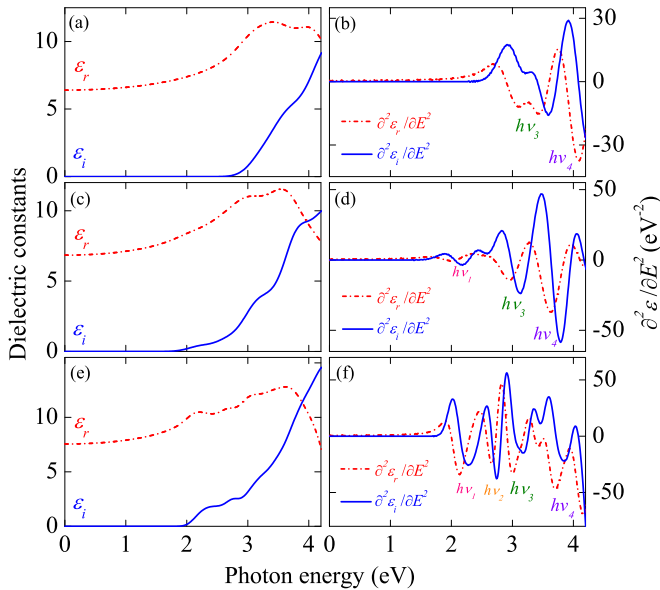


FIG. 8. (Color online) Theoretical dielectric constants and the corresponding second partial derivatives of (a),(b) rhombohedral, (c),(d) tetragonal, and (e),(f) cubic  $\text{Pb}(\text{Zn}_{1/3}\text{Nb}_{2/3})\text{O}_3$ .

the tetragonal case, respectively. The redshift of optical band gaps is closely related to the decrease of approximately 1 eV ( $h\nu_3 - h\nu_1$ ) in tetragonal phase for the bottom energy level of conducting Pb-6*p*, Nb-4*d*, and O-2*p* states compared to the rhombohedral phase, which can be associated to the disappearance of octahedrons' distortion caused by the ferroelectric polarization tilting from [111] to [001] direction. The distortions of ( $\text{NbO}_6/\text{ZnO}_6$ ) octahedrons in rhombohedral PZN tend to increase the energy difference between valance and conduction bands. However, the disappearance of distortions reduces the band gap as the polarization direction rotating to [001] direction, i.e., the tetragonal phase. Similarly, the optical band gap of cubic PZN (with energy of 1.900 eV), whose leading transition is from the hybridization O-2*p* and Pb-6*s* to conducting Nb-4*d<sub>xy</sub>*, is close to that of tetragonal phase due to undistorted ( $\text{NbO}_6/\text{ZnO}_6$ ) octahedrons. The approximate difference of about 0.2 eV for the absorption edges between the tetragonal and cubic phases can be derived from the two-degenerate O-2*p<sub>x</sub>* (or equivalently O-2*p<sub>y</sub>*) and the nondegenerate O-2*p<sub>z</sub>* states uniting into three-degenerate O-2*p* states. Furthermore, an additional absorption peak for cubic phase has been reproduced at about 2.34 eV [the cause of  $h\nu_2$  in Fig. 8(f)], which can be attributed to the electronic transitions from O-2*p* to conducting Nb-4*d<sub>xz</sub>*. In principle,

most of the interband transitions from temperature-dependent ellipsometric spectra can be well testified by the density functional theory calculations. It indicates that the variations of electronic transitions can be directly applied to judge the phase transformations in ferroelectric oxides.

#### IV. CONCLUSIONS

Temperature-dependent polarized Raman scattering indicates that the rhombohedral-tetragonal, tetragonal-cubic transformation temperatures, and intermediate temperature are about 360, 440, and 510 K, respectively. The Raman mode near  $270\text{ cm}^{-1}$  has a shift towards lower wave numbers and its integrated intensity decreases on heating due to a reduction of polar shifts about Nb(Zn, Ti)-site cations to a certain extent as well as the unit-cell expansion. The appearance of phase transformations were confirmed by the various trends of electronic transitions in peak positions and broadenings. Moreover, the redshift behavior of the transition  $h\nu_3$  at about 3.7 eV as a function of temperature follows the Bose-Einstein law due to the electron-phonon interactions and lattice thermal expansion. Finally, the redshift of absorption edges in the process of transformation from rhombohedral phase to tetragonal phase and an additional absorption peak during the tetragonal-cubic phase transition are observed. First-principles calculations reproduce the experimental results and explain them. Accurately, the  $h\nu_1$ ,  $h\nu_2$ , and  $h\nu_3$  are derived from O-2*p<sub>z</sub>* or/and Pb-6*s* to Nb-4*d<sub>xy</sub>*, Nb-4*d<sub>xz</sub>*, and Nb-4*d<sub>xy</sub>*, respectively. In brief, the experimental and theoretical results clearly suggest that the phase transformation in ferroelectric materials could be discovered by noncontact and nondestructive optical methods.

#### ACKNOWLEDGMENTS

One of the authors (J.Z.Z.) is grateful to Dr. Lin Sun, Dr. Yuanyuan Zhang, and Dr. Jun Qian for the technical supports. This work was financially supported by Major State Basic Research Development Program of China (Grants No. 2011CB922200 and No. 2013CB922300), Natural Science Foundation of China (Grants No. 11374097, No. 61376129, and No. 61125403), Projects of Science and Technology Commission of Shanghai Municipality (Grants No. 14XD1401500, No. 13JC1402100, No. 13JC1404200, and No. 15YF1413900), and the Program for Professor of Special Appointment (Eastern Scholar) at Shanghai Institutions of Higher Learning, and Project funded by China Postdoctoral Science Foundation (Grant No. 2014M560357).

- [1] R. F. Service, *Science* **275**, 1878 (1997).
- [2] N. Waesermann, B. J. Maier, B. Mihailova, R. J. Angel, J. Zhao, M. Gospodinov, C. Paulmann, N. Ross, and U. Bismayer, *Phys. Rev. B* **85**, 014106 (2012).
- [3] W. Ren, S.-F. Liu, and B. K. Mukherjee, *Appl. Phys. Lett.* **80**, 3174 (2002).
- [4] J. Cheng, Y. Yang, Y.-H. Tong, S.-B. Lu, J.-Y. Sun, K. Zhu, Y.-L. Liu, G. G. Siu, and Z. K. Xu, *J. Appl. Phys.* **105**, 053519 (2009).
- [5] B. Srimathy, R. Jayavel, S. Ganesamoorthy, I. Bhaumik, A. K. Karnal, V. Natarajan, E. Varadarajan, and J. Kumar, *Cryst. Res. Technol.* **47**, 523 (2012).
- [6] B. K. Singh, K. Kumar, N. Sinha, and B. Kumar, *Cryst. Res. Technol.* **44**, 915 (2009).
- [7] B. Noheda, D. E. Cox, G. Shirane, S. E. Park, L. E. Cross, and Z. Zhong, *Phys. Rev. Lett.* **86**, 3891 (2001).

- [8] D. La-Orautapong, B. Noheda, Z. G. Ye, P. M. Gehring, J. Toulouse, D. E. Cox, and G. Shirane, *Phys. Rev. B* **65**, 144101 (2002).
- [9] C. J. He, F. Xu, J. M. Wang, C. L. Du, K. J. Zhu, and Y. W. Liu, *J. Appl. Phys.* **110**, 083513 (2011).
- [10] Y. Barad, Y. Lu, Z.-Y. Cheng, S.-E. Park, and Q. M. Zhang, *Appl. Phys. Lett.* **77**, 1247 (2000).
- [11] N. Waeselmann, B. Mihailova, B. J. Maier, C. Paulmann, M. Gospodinov, V. Marinova, and U. Bismayer, *Phys. Rev. B* **83**, 214104 (2011).
- [12] P. S. Dobal, R. S. Katiyar, and C. S. Tu, *J. Raman Spectrosc.* **34**, 152 (2003).
- [13] O. Svitelskiy, D. La-Orautapong, J. Toulouse, W. Chen, and Z. G. Ye, *Phys. Rev. B* **72**, 172106 (2005).
- [14] K. K. Mishra, A. K. Arora, S. N. Tripathy, and D. Pradhan, *J. Appl. Phys.* **112**, 073521 (2012).
- [15] S. Kamba, E. Buixaderas, J. Petzelt, J. Fousek, J. Nosek, and P. Bridenbaugh, *J. Appl. Phys.* **93**, 933 (2003).
- [16] E. W. Sun, R. Zhang, Z. Wang, D. P. Xu, L. Li, and W. W. Cao, *J. Appl. Phys.* **107**, 113532 (2010).
- [17] J. Y. Xu, J. Tong, M. L. Shi, A. H. Wu, and S. J. Fan, *J. Cryst. Growth* **253**, 274 (2003).
- [18] M. Jin, J. Y. Xu, M. L. Shi, and S. J. Fan, *J. Phys. D: Appl. Phys.* **40**, 1473 (2007).
- [19] A. Dubroka, J. Humlíček, M. V. Abrashev, Z. V. Popović, F. Sapiña, and A. Cantarero, *Phys. Rev. B* **73**, 224401 (2006).
- [20] P. E. Blöchl, *Phys. Rev. B* **50**, 17953 (1994).
- [21] G. Kresse and J. Furthmüller, *Comput. Mater. Sci.* **6**, 15 (1996).
- [22] H. J. Monkhorst and J. D. Pack, *Phys. Rev. B* **13**, 5188 (1976).
- [23] N. Choudhury, Z. Wu, E. J. Walter, and R. E. Cohen, *Phys. Rev. B* **71**, 125134 (2005).
- [24] Y. Yan, S. J. Pennycook, Z. Xu, and D. Viehland, *Appl. Phys. Lett.* **72**, 3145 (1998).
- [25] W.-Y. Tong, H.-C. Ding, Y.-C. Gao, S.-J. Gong, X. G. Wan, and C.-G. Duan, *Phys. Rev. B* **89**, 064404 (2014).
- [26] E. H. Kisi, J. S. Forrester, and K. S. Knight, *Acta Crystallogr. Sect. C* **62**, i46 (2006).
- [27] A. Kiraci and H. Yurtseven, *Ferroelectrics* **450**, 93 (2013).
- [28] M. R. Shen, G. G. Siu, Z. K. Xu, and W. W. Cao, *Appl. Phys. Lett.* **86**, 252903 (2005).
- [29] R. M. A. Azzam and N. M. Bashara, *Ellipsometry and Polarized Light* (North-Holland, Amsterdam, 1977).
- [30] A. B. Djurišić, Y. Chan, and E. H. Li, *Mater. Sci. Eng., R* **38**, 237 (2002).
- [31] D. A. G. Brügge, *Ann. Phys. (Leipzig)* **416**, 636 (1935).
- [32] P. Lautenschlager, M. Garriga, L. Viña, and M. Cardona, *Phys. Rev. B* **36**, 4821 (1987).
- [33] X. L. Zhang, Z. G. Hu, G. S. Xu, J. J. Zhu, Y. W. Li, Z. Q. Zhu, and J. H. Chu, *Appl. Phys. Lett.* **103**, 051902 (2013).
- [34] T. Huang, Z. G. Hu, G. S. Xu, X. L. Zhang, J. Z. Zhang, and J. H. Chu, *Appl. Phys. Lett.* **104**, 111908 (2014).
- [35] M. Rössle, C. N. Wang, P. Marsik, M. Yazdi-Rizi, K. W. Kim, A. Dubroka, I. Marozau, C. W. Schneider, J. Humlíček, D. Baeriswyl, and C. Bernhard, *Phys. Rev. B* **88**, 104110 (2013).
- [36] F. F. Xin, Z. H. Zhai, X. J. Wang, Y. F. Kong, J. J. Xu, and G. Q. Zhang, *Phys. Rev. B* **86**, 165132 (2012).
- [37] M. Siewattana and D. J. Singh, *Phys. Rev. B* **73**, 224105 (2006).